Original Article
cnj.araku.ac.ir

Cite This: Colloid Nanosci. J. 3(1) (2025) 499-518 DOI: 10.61882/CNJ.3.1.499

Core-shell Fe-cross-linked Biopolymer as Nanohybrid Catalyst and Ni Particle: Kinetics and Thermodynamics of Hydrogen Generation via $NaBH_4$ Hydrolysis

Mona Jalali Rad, Mohammad Hassan Loghmani*

Department of Nanotechnology, Faculty of Engineering, University of Guilan, Rasht, Iran

ARTICLE INFO

Article History:
Received Apr 23, 2025
Revised May 12, 2025
Accepted May 12, 2025
Published July 15, 2025

Corresponding Authors:
Mohammad Hassan Loghmani
Email:
mhmdloghmani@guilan.ac.ir

ABSTRACT

In this work, Fe and Ni supported on extracted Glucomannan (Glu) from Orchis Mascula roots were prepared. N,N'-Methylenebisacrylamide as a cross-linker and methacrylic acid as a monomer were used to convert soluble extract to insoluble glucomannan. Synthesized catalysts were characterized by XRD, XPS, FE-SEM, EDS, and TEM techniques. Significant TEM shows polymer chains formed as a circular structure including metal/metal boride species. Indeed, iron particles are entrapped in the cavities of glucomannan polymer as a core-shell structure. Average size of the entrapped Fe is 11 nm while Ni particle is 256 nm. The efficacy of the synthesized catalysts is evaluated for hydrogen production. Kinetic investigations were conducted to ascertain the partial order concerning catalyst dosage and $NaBH_4$ concentration. Results cleared that totally order of hydrolysis reaction is approximately near to 1 and 1.5 for Fe/Glu and Ni/Glu, respectively. The activation energy values of Fe/Glu and Ni/Glu catalysts were estimated at 28 and 63 kJ/mol, respectively. $\Delta H^{\#}$ and $\Delta S^{\#}$ values of Fe/Glu and Ni/Glu catalysts were calculated at 35.75 kJ/mol and -170.6 J/molK and 74.41 kJ/mol and -63.8 J/molK, respectively.

KEYWORDS: *Hydrolysis; kinetics; thermodynamics; Glucomannan; hydrogen generation; sodium borohydride*

1. Introduction

Hydrogen is the most abundant element on Earth, though it is rarely found in its pure form. This means that for hydrogen production, it must be extracted from compounds. Hydrogen can be generated from diverse local resources, including fossil fuels, water electrolysis, and biomass. The environmental impact and energy efficiency of hydrogen production depend on the method used. Although hydrogen extraction from its sources requires energy, hydrogen gas has significant potential as a clean energy source. When hydrogen gas is burned with oxygen, only water is produced. Thus, hydrogen is considered a preferable energy source compared to others due to its minimal pollutant emissions. Metal hydrides, which serve as hydrogen storage materials, have high volumetric hydrogen capacity and can act as hydrogen production sources through hydrolysis or methanolysis reactions. Several boron hydrides, such as NH_3BH_3 [1], $LiAlH_4$ [2], KBH_4 [3], and $NaBH_4$ [4], have been used for hydrogen generation via these reactions. $NaBH_4$ has received considerable attention from scientists due to its high theoretical gravimetric hydrogen capacity (10.8%). However, under ambient conditions, the overall conversion efficiency of $NaBH_4$ self-hydrolysis reaction is only 7–8% [5], necessitating the use of catalysts. Nanoscale transition metals are promising alternatives to noble metals. Hani Nasser Abdelhamid compiled a comprehensive list of catalysts and reaction conditions [6]. Notable catalysts include Co-B [7], Ni–W–P/γ-Al_2O_3 [8], Ni-B [9], Ni [10], Ni-Ag [11], Ni-Co-B [12], Ni-Fe-B [13], Ni-B–silica [14], Co-Ni [15], Co-Mo [16], Fe-$Fe_2(MoO_4)_3$ [17], hierarchical porous ZIF-8 [18], Co-W-P [19], Co-B hollow spheres

[20], Co-Mn-B [21], Co-Ce-B [22], CoWB/NF nanodendrite [23], Co-Ni-P [24], Ni-Ni_3B [25], Fe_3O_4@C-Co [26], Fe_2O_3 [27], Cu-Fe-B [28], Co–Fe–B [29], Fe-B-P [30], Co-Ni-Fe-P [31] and Co-Mo-tudies, various materials have been employed as supports, including Mo-B [32] which play effective roles in hydrogen generation. However, excessive nanoparticle agglomeration reduces surface energy and stabilizes particles through relaxation. Thus, supports should be used to stabilize particles. Indeed, the number of active sites on the catalyst surface increases, which prevents agglomeration. As evidenced by published studies, various materials have been employed as supports, including MWCNTs/IL/Mn nanohybrids [33], ionic liquids [34], magnetic activated carbon [35], magnetite-MWCNTs [36], PVDF [37], p(SPM) hydrogel matrix [38], wheat straw cellulose [39], p(ethylene imine) [40], Na-exchanged bentonite clays [41], dandelion-like CNTs-Ni foam composites [42], zeolite-HCl [43], Mod-p(AAm) [44], PAN nanofibers [45], open-CNTs [46], porous SiO_2 [47], ZIF-9 [48], Co@ZIF-8 [49], carbon composites [50,51], p(vinyl imidazole) [52,53], and p(HEMA) cryogels [54]. Glucomannan is a water-soluble polysaccharide and fermentable nutritive fiber composed of β-D-mannose and α-D-glucose units linked by β-1,4 glycosidic bonds. It offers several advantages, such as low cost, non-toxicity, biocompatibility, natural abundance, and gelling properties [55]. To utilize glucomannan as a natural polymer network for immobilizing metal catalysts, it must be chemically modified using a crosslinker. During crosslinking, a three-dimensional (3D) polymer network forms, rendering glucomannan insoluble. Glucomannan can be extracted from Salep (Orchis mascula) roots, a process pioneered by Ali Pourjavadi, who developed superabsorbent hydrogels from Salep [56]. To the best of our knowledge, no studies have reported the use of glucomannan (derived from Orchis mascula)-supported Ni/Fe catalysts for hydrogen generation via $NaBH_4$ hydrolysis. Our group has extensive expertise in hydrogen generation reactions, as demonstrated in prior publications [26,57–62], including recent work on Co-glucomannan nanoparticles [63]. In this study, we aim to employ a natural polymer—easily extracted from plants—as a support to stabilize Fe/Ni nanostructures for catalytic applications. Remarkably, the polymer chains encapsulate the iron particles, forming a core-shell morphology. Specifically, Fe and Fe-boride species are entrapped within glucomannan cavities during synthesis. The synthesis process involves two key steps: (i) extraction of glucomannan from Orchis mascula roots and (ii) dispersion and stabilization of Fe/Ni nanoparticles on the biopolymer matrix during catalyst preparation. We propose Fe(Ni)-glucomannan as a heterogeneous catalyst for $NaBH_4$ hydrolysis. To immobilize Fe/Ni nanoparticles on the glucomannan matrix, N,N’-methylenebisacrylamide (MBA) was used as a crosslinker, and methacrylic acid (MAA) as a monomer, to convert the soluble extract into an insoluble polymer network. The synthesized catalysts were characterized by XRD, XPS, SEM, and TEM. Their activity in hydrogen production via $NaBH_4$ hydrolysis was evaluated, and kinetic studies were conducted to determine the reaction order and rate law. Key parameters—initial $NaBH_4$ concentration, catalyst dosage, and temperature—were systematically analyzed. The activation energy for each catalyst was calculated using the Arrhenius equation (see Results section).

2. Experimental

2.1. Materials and method

All chemical materials were used without any purification. The orchid root was purchased from a traditional herbal shop in Kurdistan province, Iran. Methacrylic acid (MAA), N, N’-Methylenebisacrylamide (MBA), $FeCl_3.6H_2O$, $NiCl_2.6H_2O$, potassium persulfate (KPS), ethanol, acetone and $NaBH_4$ were obtained from Merck.

2.2. Glucomannan extraction and Catalysts synthesis

Glucomannan polymer was isolated from dried orchid roots (purchased from a local market) using a two-step extraction process, as previously reported [63]. Initially, a measured quantity of roots was heated in deionized water at 60 °C, followed by removal, peeling, and a two-step drying process (2 hours at 60 °C and 15 minutes at 140 °C). The dried roots were then ground into a powder and reheated in deionized water at 40 °C for 1 hour. Subsequently, an equal volume of ethanol was added to precipitate glucomannan, forming a gel. The gel was filtered, washed sequentially with deionized water and acetone, and air-dried at ambient temperature. For catalyst synthesis (Scheme 1), a homogeneous

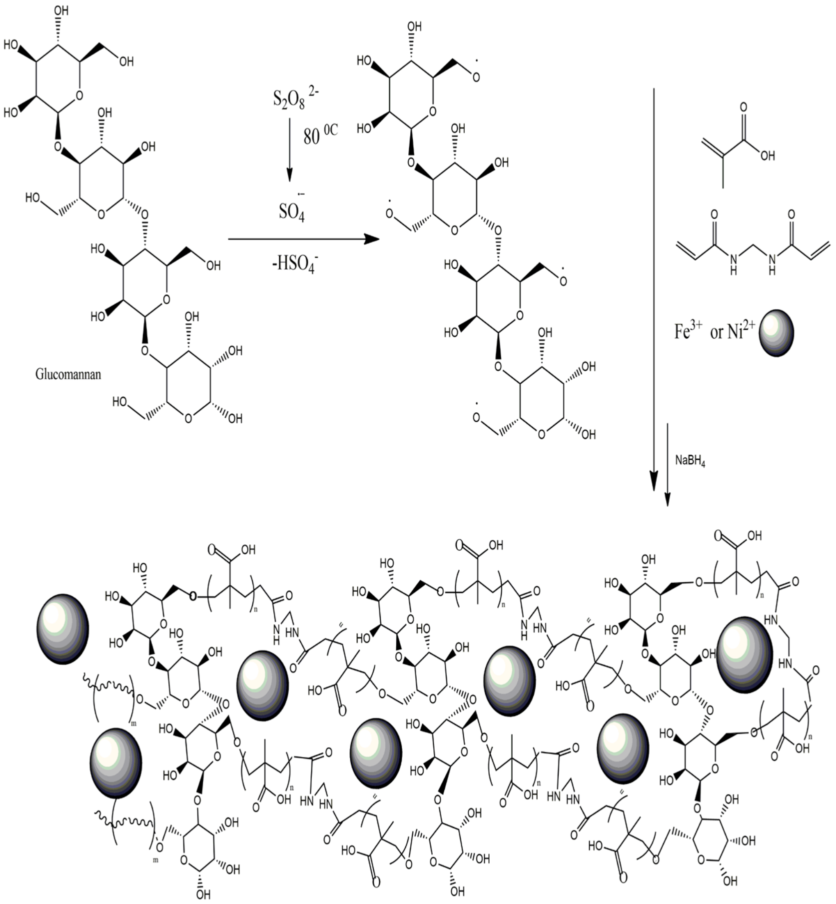

Scheme 1. Synthesis procedure of cross-linked Glucomannan-nano catalyst

solution was first prepared by dissolving 1 g of glucomannan in 100 mL deionized water at 45 °C for 20 minutes. $FeCl_3{\cdot}6H_2O$ or $NiCl_2{\cdot}6H_2O$ (1 mmol in 3 mL H_2O) was added to the solution, followed by sequential addition of MBA (0.2 mmol, 0.036 g in 3 mL H_2O) and MAA (1 mmol, 80 µL in 3 mL H_2O). After thorough mixing, potassium persulfate (KPS, 1 mmol, 0.270 g in 3 mL H_2O) was introduced. The temperature was then raised to 80 °C to activate KPS, and after 30 minutes, a $NaBH_4$ solution (5 mmol, 189 mg in 3 mL H_2O) was added dropwise to complete the synthesis.

Upon addition of the sodium borohydride ($NaBH_4$) solution, the solution's color shifted from green to black, indicating successful reduction of metal ions. After complete reduction, the reaction mixture was precipitated by ethanol addition. The precipitate was then washed sequentially with acetone and deionized water and vacuum-dried overnight at room temperature. The synthesized nanocatalysts were stored in an airtight container for subsequent hydrogen generation experiments.

2.3. Catalysts characterization

The phase of catalysts was recognized by XPert PRO MPD, PAnalytical Company. XRD pattern was recorded using Cu Kα radiation in the 2θ range of 30-60. The surface morphology of powders was seen by the field emission scanning electron microscope (FE-SEM-MIRA III TESCAN). Sputter coating for preparation of sample through SEM analysis was done by metallic Au. Also, the shape of the best catalyst was examined on transmission electron microscopy (TEM-EM 208S).

2.4. Hydrogen generation

The catalytic activity of the synthesized powder was evaluated via the hydrolysis reaction of sodium borohydride ($NaBH_4$). Hydrogen gas

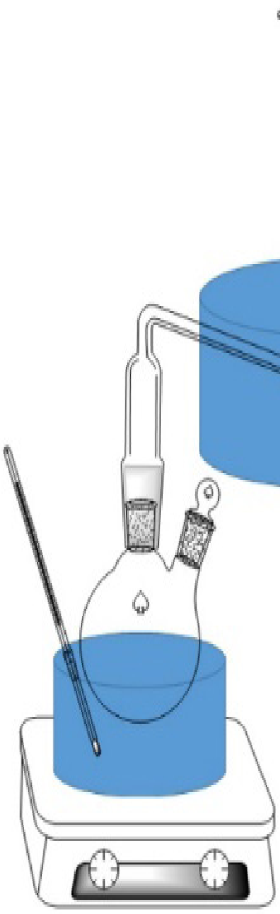

Scheme 2. Setup of hydrogen generation and measuring

evolution was monitored using a custom-designed gasometric setup (Scheme 2), where an inverted graduated cylinder filled with water quantified the liberated H_2 volume. In a typical experiment, a measured amount of catalyst was loaded into a two-neck round-bottom flask, followed by the addition of an alkaline $NaBH_4$ solution (2 wt.% NaOH) under controlled temperature. Both necks were securely sealed, and H_2 gas evolution commenced immediately upon $NaBH_4$ introduction. The displaced water volume in the cylinder, recorded at fixed time intervals, directly correlated with the H_2 yield. Notably, the self-mixing effect induced by H_2 bubble formation eliminated the need for mechanical stirring. To investigate reaction kinetics, key parameters were systematically varied: initial $NaBH_4$ concentration (1.25–20 wt.%), catalyst dosage (25–125 mg), and temperature (308, 318, and 328 K).

3. Results and discussion

3.1. Characterization

Fig. 1 shows the XRD pattern of glucomannan-supported nanocatalysts. For comparison, reference patterns for Fe_2O_3, Fe_2O_3, and metallic Fe are included in Fig. 1(a). The experimental pattern exhibits multiple peaks, some of which align with JCPDS cards (see Fig. 1(b)). However, precise phase identification remains challenging due to potential overlaps. Given the use of $NaBH_4$ in the synthesis (as detailed in the Experimental section), the presence of both metallic Fe and iron borides (e.g., Fe_2B, FeB) is anticipated. Peaks at 2θ = 35°, 41°, and 45° are tentatively assigned to Fe_2B (200), FeB (111), and α-Fe (110), respectively [64–67]. Fig. 1(c) displays the XRD pattern of Ni/Glu catalyst. No peaks corresponding to nickel oxide phases are observed, which aligns with the expected reduction of Ni^{2+} ions by $NaBH_4$ to form metallic Ni (0) and

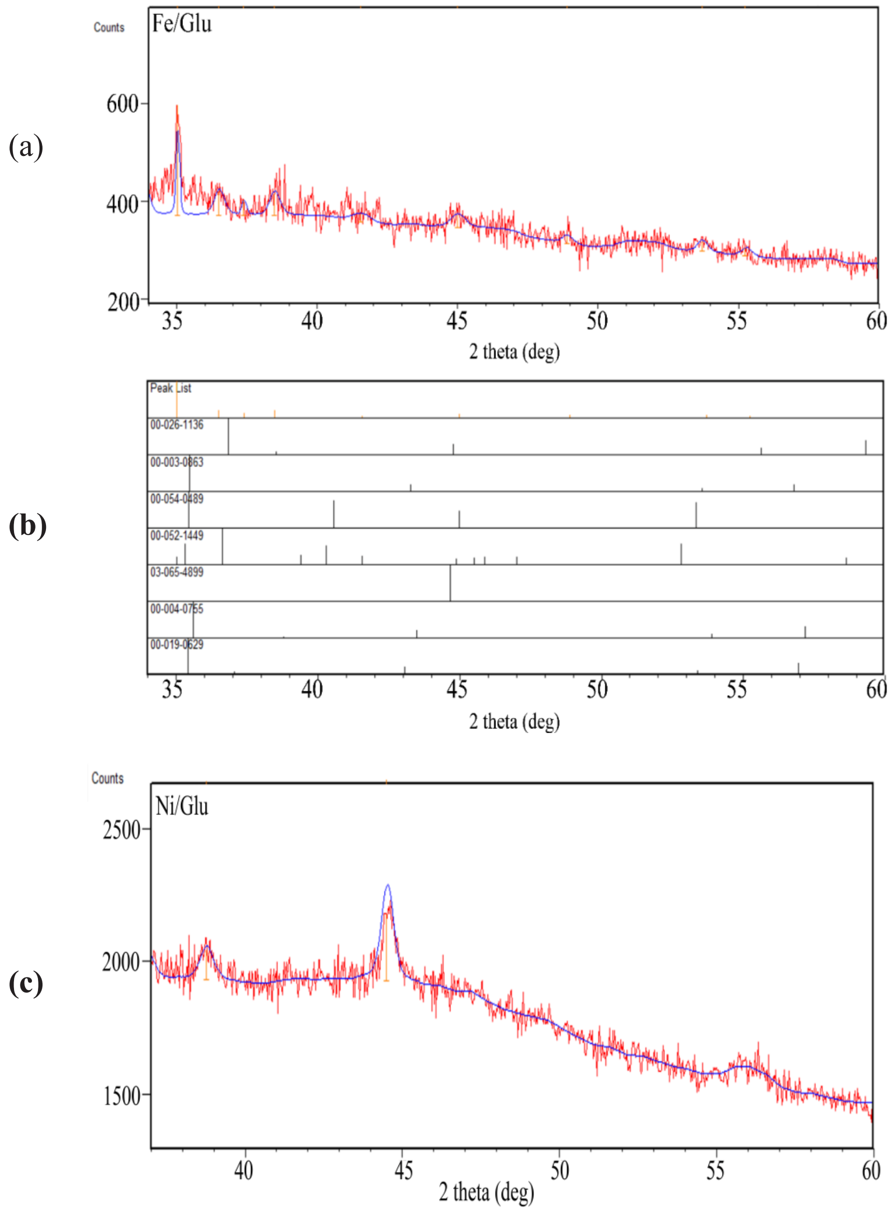

Fig. 1. XRD patterns of **(a)** Fe/Glu, **(b)** JCPDS cards and **(c)** Ni/Glu catalyst

nickel borides. Peaks at 2θ = 38.71°, 44.55°, 51.82°, and 56.06° are attributed to Ni_3B, Ni (111), Ni (200), and Ni_4B_3, respectively [

XPS analyses confirmed the presence of Fe, Ni, and B on the catalyst surface, consistent with the synthesis protocol. Fig. 2 displays high-resolution Fe 2p, Ni 2p, and B 1s spectra. The Fe 2p spectrum (Fig. 2a) exhibits three prominent peaks at 706.1 eV, 711.5 eV, and 724.3 eV, assigned to Fe^0 $2p_3/_2$, Fe^{2+} $2p_3/_2$, and Fe^{2+} $2p_1/_2$, respectively [69, 70]. The absence of Fe^{3+} species, which typically appear near 715 eV for Fe^{3+} $2p_3/_2$, confirms the reductive synthesis conditions favoring partial reduction of Fe precursors to metallic Fe^0. Satellite peaks at 718.8 eV and 734 eV, characteristic of Fe^{2+}, further validate this assignment and exclude significant contributions from Fe^{3+}. The observed Fe^{2+} oxidation state likely originates from surface oxidation during post-synthesis air exposure. The Ni 2p spectrum (Fig. 2b) reveals two dominant peaks at 852.5 eV (Ni^0 $2p_{3}/_{2}$) and 870.1 eV (Ni^0 $2p_{1}/_{2}$), confirming metallic nickel. Minor peaks at 858.1 eV (Ni^{2+} $2p_{3}/_{2}$) and 875 eV ($Ni^{2+}2p_{1}/_{2}$) suggest superficial oxidation of Ni^0 during sample handling. The coexistence of Ni^0 and Ni^{2+} aligns with prior studies reporting surface oxidation of Ni-based catalysts exposed to ambient conditions [71]. The dominance of Ni^0 signals indicates that the bulk structure remains metallic, consistent with the reducing synthesis environment. The B1s spectrum (Fig. 3) deconvoluted into two peaks: a lower binding energy component (188–191.8 eV) attributed to metal borides (Fe-B/Ni-B), confirming boron incorporation into the catalyst structure, and a higher binding energy peak (192–192.2 eV) assigned to boron oxo-species (B-O) formed via surface oxidation upon air exposure [72]. The slight variation in the boride peak positions (188 eV vs. 191.8 eV) reflects differences in electronegativity between Fe and Ni in their respective borides. The coexistence of Fe^{2+} and Ni^0 suggests a synergistic redox-active surface, where Fe^{2+} may act as Lewis acid sites, while metallic Ni^0 facilitates electron transfer. This interplay is critical for catalytic applications, such as hydrogen evolution. The presence of surface-oxidized species (Fe^{2+}, Ni^{2+}, B-O) highlights the importance of controlled synthesis and storage conditions to minimize undesired oxidation.

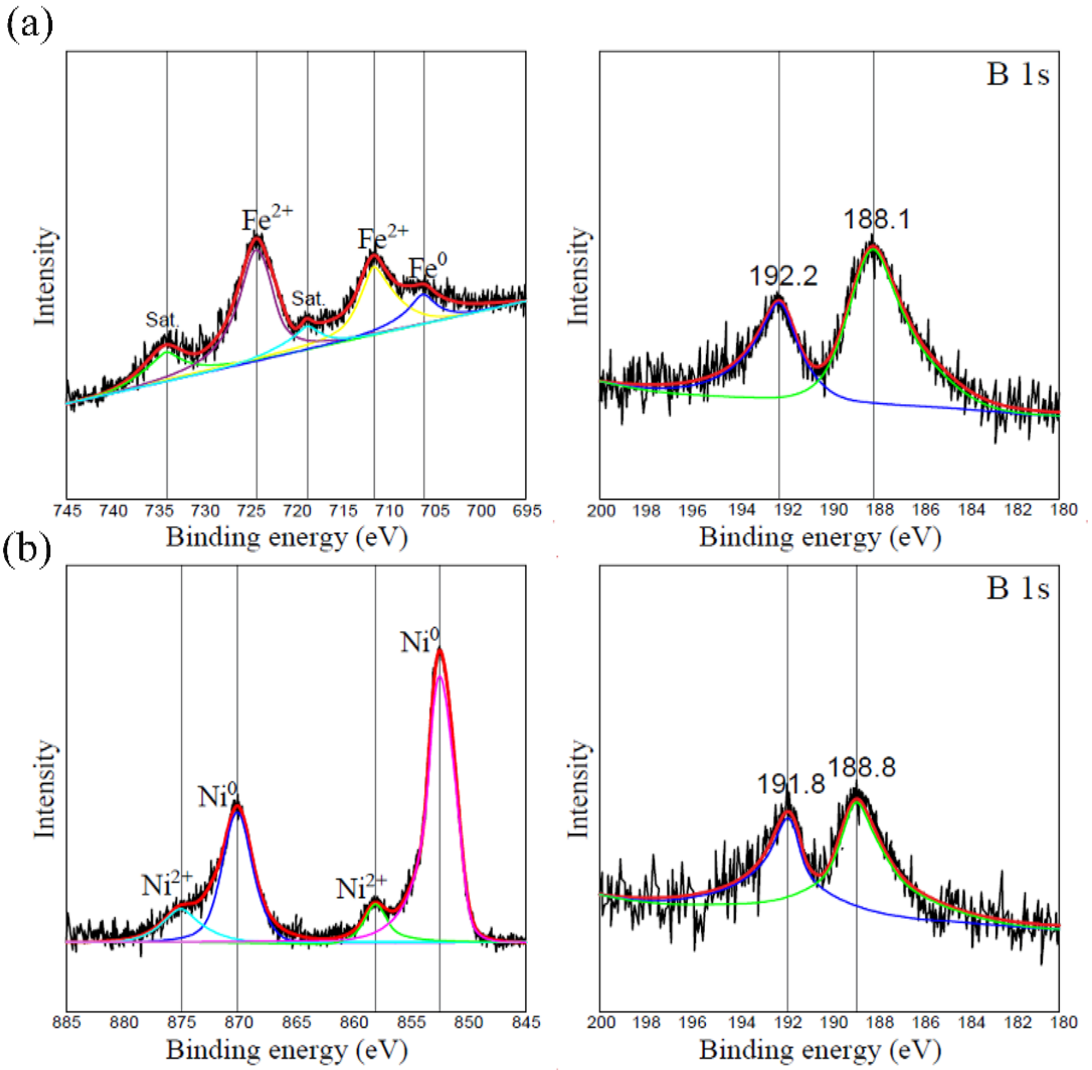

Fig. 2. XPS spectra o **(a)** Fe/Glu and **(b)** Ni/Glu

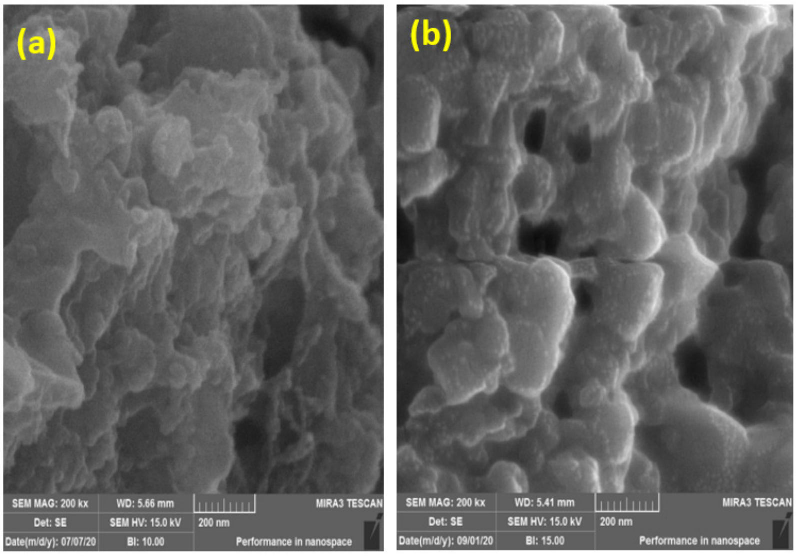

Fig 3. SEM images of **(a)** Fe/Glu and **(b)** Ni/Glu powders

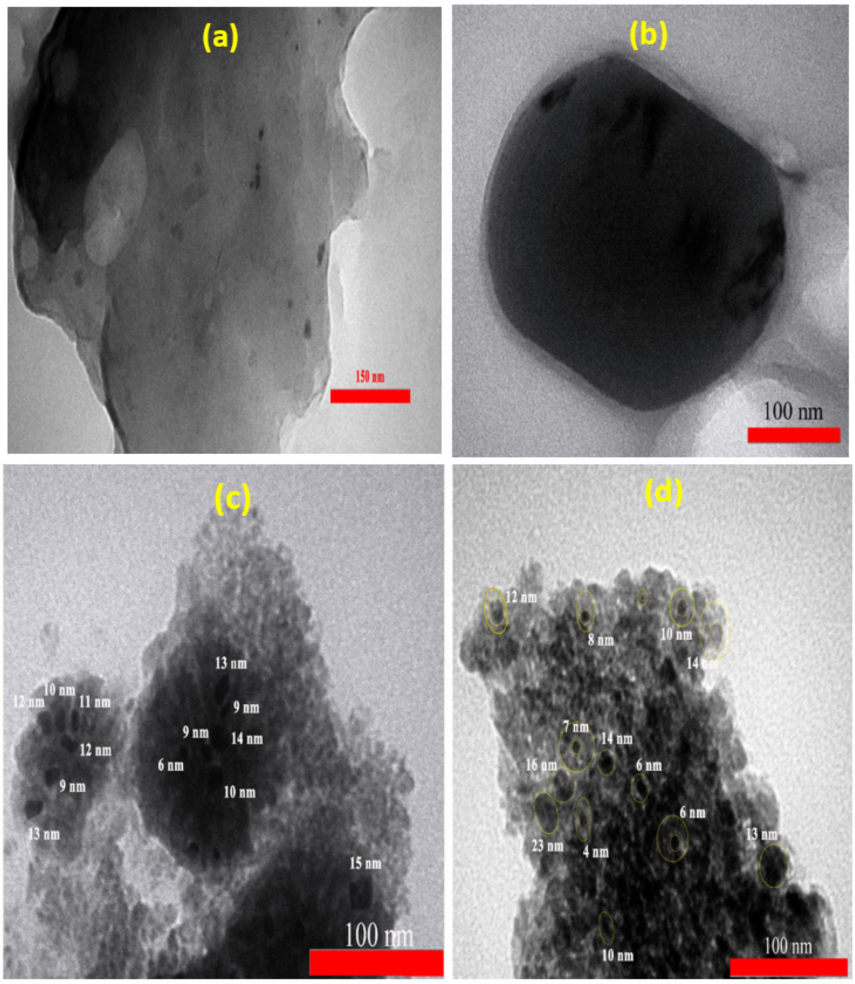

Fig. 4. TEM images of **(a)** cross-linked Glu, **(b)** Ni/Glu and (c & d) Fe/Glu powders

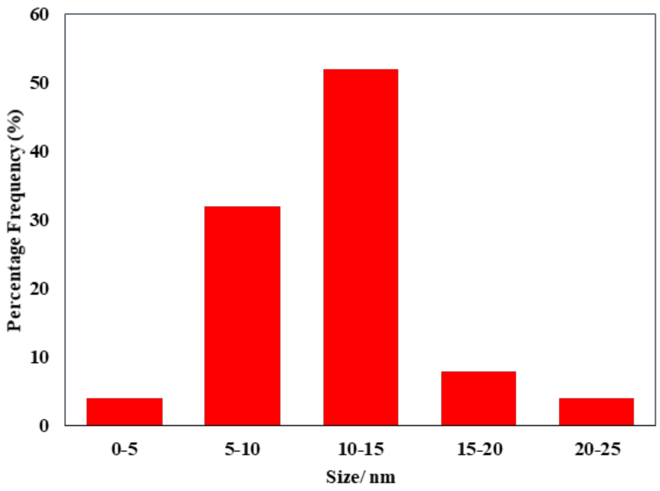

Fig. 5. Particle size distribution of Fe/Glu catalyst.

The dimensions and morphology of the obtained catalyst powders were analyzed using FE-SEM and TEM methods. The findings are illustrated in Fig. 3. FE-SEM pictures are presented at a magnification of 200,000x. The FE-SEM pictures of Fe/Glu and Ni/Glu demonstrate that the polymer is produced at the nanoscale. Nonetheless, distinguishing between polymer and metal particles is unfeasible. Owing to the constraints of the FE-SEM microscope, implement exact modifications and obtain crisp images of the particles.

Fig. 4 shows TEM images of extracted Glu, Ni/Glu and Fe/Glu powders. Cross-linked glucomannan polymer is shown in Fig. 4. (a). No specific morphology or specific particle is seen. For more consideration it is tried to show two micrographs of Fe/Glu powder. It can be found that polymer chains formed as a circular structure including metal/metal boride species. It is like a core-shell matrix. As seen, iron particles are entrapped in the cavities of glucomannan polymer. Fig. 4. (b) depicts Ni/Glu particles are much bigger than Fe/Glu. So, it can probably effect on catalytic activity. The black region is attributed to the metal particles. The particle size distribution (Fig 5.) of the Fe/Glu catalyst, as determined from TEM measurements, reveals a predominant population of particles within the 10–15 nm range, accounting for 52% of the total particles. A significant fraction (32%) of particles falls within the 5–10 nm range, while larger particles (15–20 nm and 20–25 nm) constitute 8% and 4%, respectively. The mean particle size is calculated to be 11 nm, reflecting the effective stabilization of nanoparticles within the glucomannan matrix. This distribution underscores the successful synthesis of a catalyst with a majority of active sites in the nanoscale regime, which is critical for enhancing surface reactivity and catalytic performance in hydrogen generation applications. Average size of the entrapped Ni particle is 256 nm. Iron ions are better dispersed in the polymer matrix than nickel ions, so it is more stable. In fact, the polymer surrounds the Fe particles better and causes the formation of smaller particles.

Also, EDS patterns and mapping images were prepared and shown in Fig. 6. It is cleared that there are C, O, B, Ni and Fe elements in region shown in image. Indeed, C and O elements belong to polymer network. Elements B and Fe are attributed to the added reagents to prepare catalyst on polymer surface. As it can be seen, Fe and Ni particles dispersed on polymer surface.

3.2. Catalytic activity of synthesized nanoparticles

The hydrolysis reaction of sodium borohydride ($NaBH_4$) was monitored using Fe/Glu and Ni/Glu catalysts, with hydrogen gas evolution serving as the primary indicator of catalytic activity. Kinetic studies were conducted to evaluate the hydrogen generation rates by systematically varying three parameters: catalyst dosage (25–125 mg), initial $NaBH_4$ concentration (1.25–20 wt.%), and reaction temperature (308–328 K). Partial reaction orders with respect to $NaBH_4$ and catalyst dosage were determined experimentally to establish the

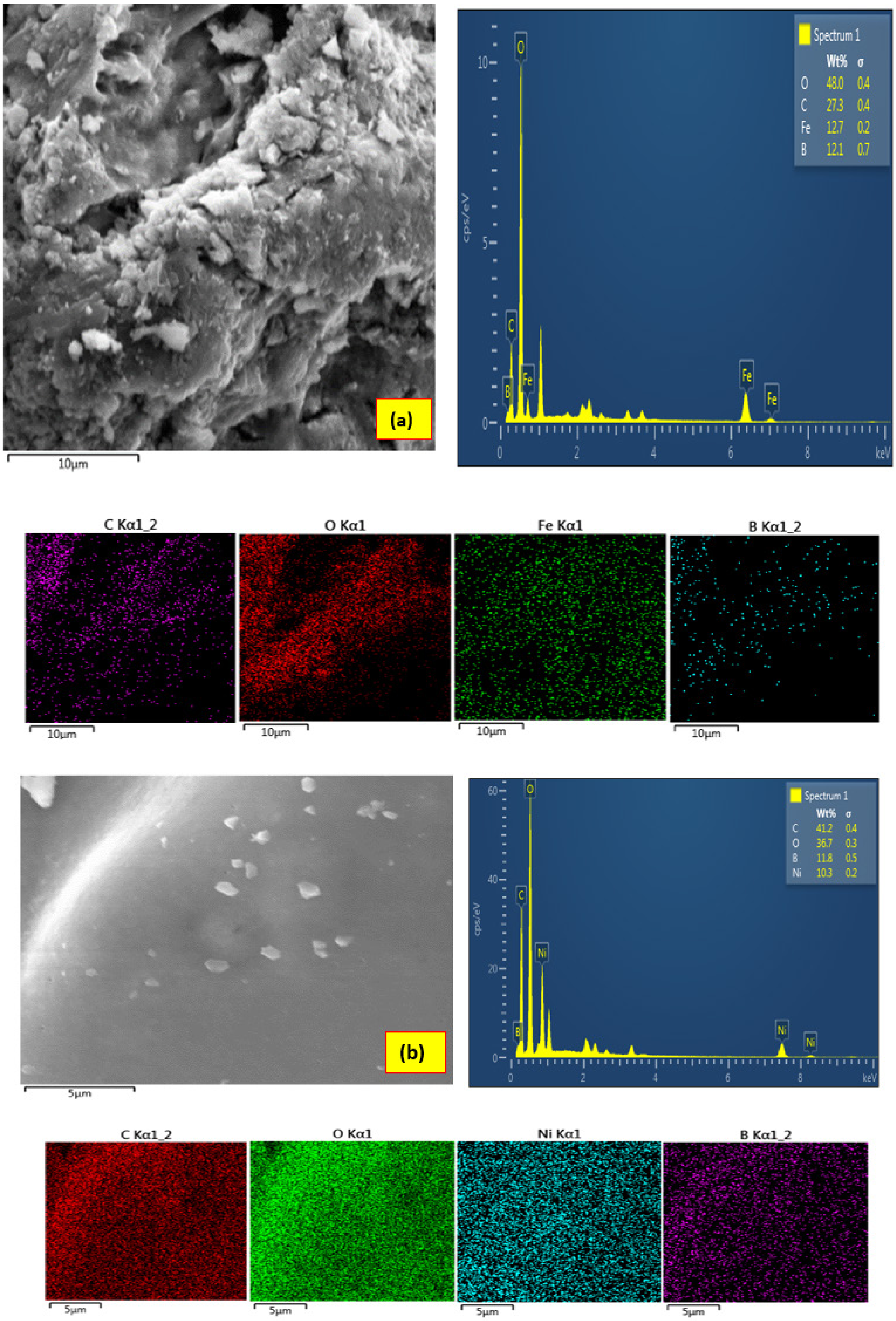

Fig. 6. EDS and mapping patterns of **(a)** Fe/Glu and **(b)** Ni/Glu

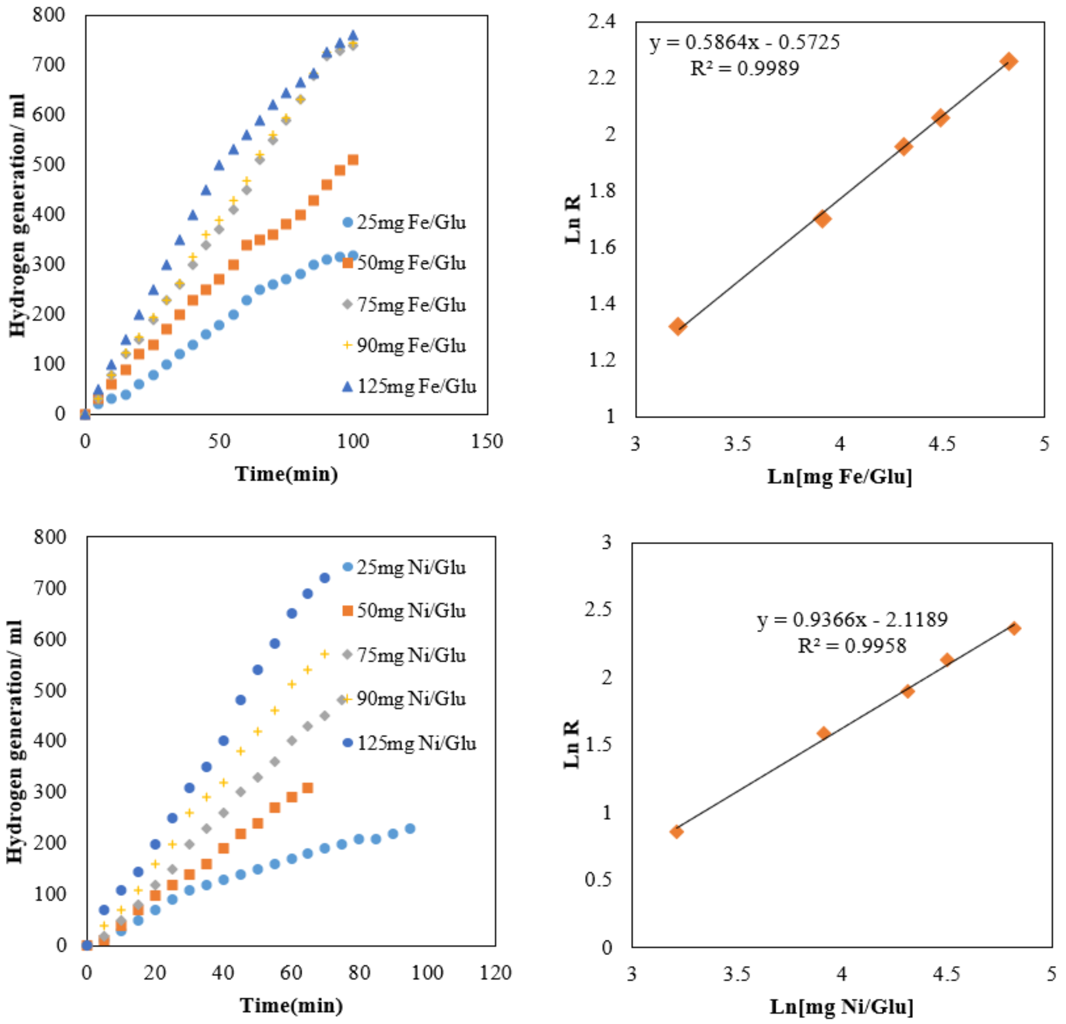

Fig. 7. The volume of hydrogen generated versus time plot and hydrogen generation rate versus the catalyst dosage (both in logarithmic scale)-effect of catalyst dosage at constant sodium borohydride (5 wt.%), NaOH (2 wt.%) and temperature 45 °C.

rate law. Activation energy (E_a) for the catalytic hydrolysis was calculated using the Arrhenius equation by analyzing rate constants derived from temperature-dependent experiments. To isolate temperature effects, reactions were performed at a fixed $NaBH_4$concentration (5 wt.%) and catalyst dosage (75 mg) across the specified temperature range. For determining the reaction order relative to $NaBH_4$ concentration, catalyst dosage and temperature were held constant at 75 mg and 318 K, respectively, while varying $NaBH_4$ concentrations (1.25–20 wt.%). Conversely, to assess the dependence on catalyst dosage, $NaBH_4$ concentration and temperature were fixed at 5 wt.% and 318 K, respectively, with catalyst amounts varied between 25–125 mg. Partial orders were derived from logarithmic plots of reaction rate versus $NaBH_4$ concentration or catalyst dosage, where the slopes of linear fits provided the respective reaction orders. To minimize confounding variables, NaOH concentration was maintained at 2 wt.%, and temperature was strictly controlled. Fig. 7 illustrates the direct correlation between catalyst dosage (Fe/Glu and Ni/Glu) and hydrogen production rate, highlighting the enhanced catalytic activity with increasing catalyst mass.

Under these circumstances, an increase in the

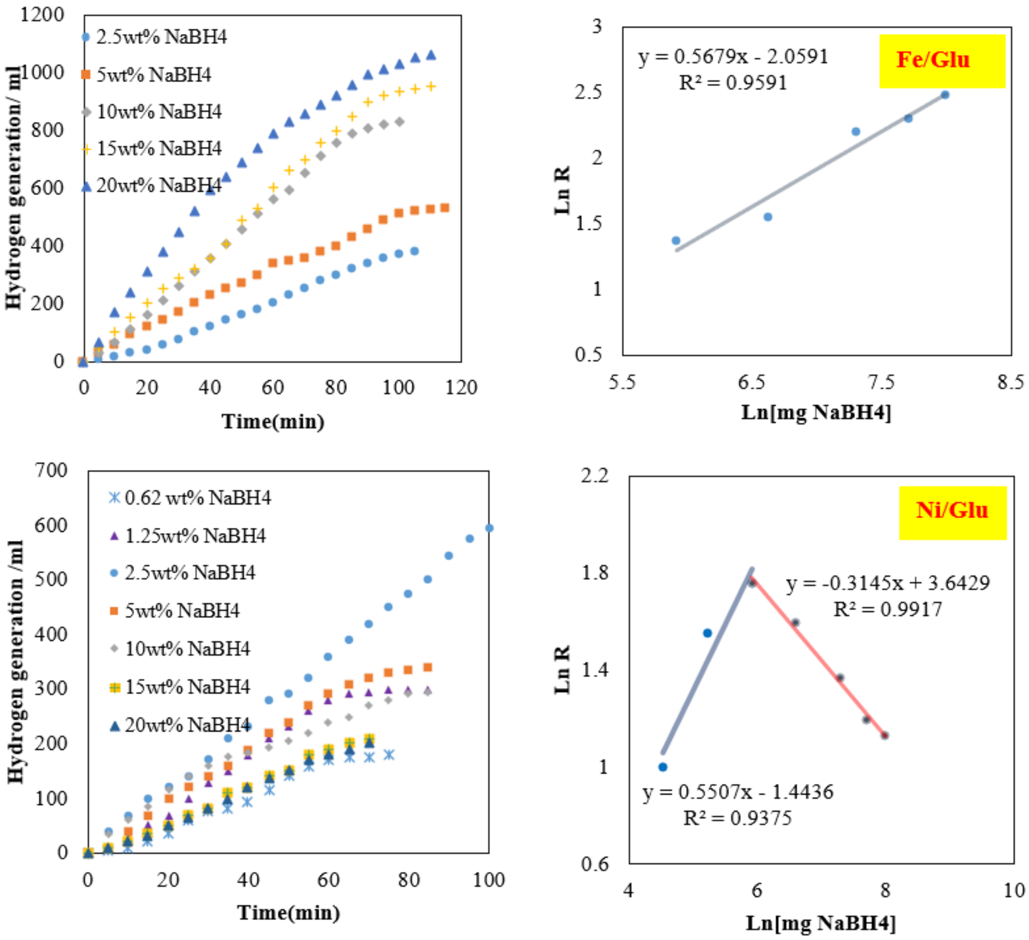

Fig. 8. The volume of hydrogen generated versus time plot and hydrogen generation rate versus the $NaBH_4$ concentration (both in logarithmic scale)- depending on the sodium borohydride concentration at constant catalyst dosage (50 mg), NaOH (2 wt.%) and temperature 45 °C.

volume of hydrogen gas produced was observed as the catalyst amount was elevated from 25 mg to 125 mg. This phenomenon was found to be specific to the Ni/Glu catalyst. The surface area of the catalyst and the amount of sodium borohydride adsorbed on it were both shown to increase with the catalyst amount. It was noted that the number of active catalytic sites responsible for sodium borohydride adsorption and subsequent hydrogen gas generation increased with the catalyst amount. To determine the reaction order with respect to the catalyst amount, a logarithmic plot of the hydrogen gas production rate was constructed. The partial reaction order of the rate law with respect to the catalyst amount was determined from the slope of the logarithmic plot. Similarly, the partial order with respect to the catalyst dosage was derived from the slope of the linear regression. The partial reaction orders for Fe/Glu and Ni/Glu were computed as 0.5864 and 0.9366, respectively, under these conditions. The initial concentration of sodium borohydride ($NaBH_4$) was identified as one of the key variables influencing the rate law equation in the hydrolysis process. To investigate the effect of $NaBH_4$ concentration on catalytic hydrolysis, a series of experiments were performed with varying $NaBH_4$ concentrations (2.5–20 wt.%) and a fixed NaOH concentration (2 wt.%), while maintaining a constant catalyst amount (50 mg) at 45 °C. Fig. 8 illustrates the hydrogen gas production rate over time for various weight percentages of sodium borohydride with Fe/Glu and Ni/Glu catalysts.

To determine the partial reaction order with respect to sodium borohydride concentration, the logarithmic plot of hydrogen gas generation rate was analyzed. An increase in $NaBH_4$concentration was expected to enhance hydrogen gas production due to the greater availability of the reactant. However, for the Fe/Glu catalyst, hydrogen gas production was observed to increase from 4 to 16 mL/min as the $NaBH_4$ concentration was raised from 2.5% to 20%. Notably, an eightfold increase in the initial $NaBH_4$ concentration resulted in only a fourfold improvement in the hydrogen release rate, indicating a sublinear relationship. In contrast, for the Ni/Glu catalyst, hydrogen gas generation was found to increase within a narrow $NaBH_4$ concentration range (0.62%–5%). Beyond this range, a decline in hydrogen production was observed when the $NaBH_4$ concentration was increased from 2.5% to 20%, consistent with previous findings reported by Kaur et al. [73].

Specifically, the hydrogen production rate decreased from 12 to 6 mL/min when the initial $NaBH_4$ concentration was doubled from 5% to 10%, demonstrating an inverse correlation. This trend persisted at higher $NaBH_4$ concentrations, suggesting catalyst surface saturation and subsequent reduction in catalytic activity. The logarithmic plot of hydrogen gas production versus initial $NaBH_4$ concentration revealed two distinct linear regimes: one with a positive slope of 0.5507 (attributed to reactant-limited conditions) and another with a negative slope of -0.3145 (associated with catalyst saturation effects). The ascending regime was utilized to derive the rate law equation, while the descending regime underscored the limitations imposed by catalyst surface saturation. A plausible explanation for this dual behavior may be attributed to the prolonged interaction time between BH_4^- ions and the catalyst surface at low sodium borohydride ($NaBH_4$) concentrations. As the $NaBH_4$ concentration increases, the concentration of sodium metaborate (a by-product) also rises, leading to its accumulation on the catalyst surface.

Consequently, active sites become obstructed, reducing catalytic efficiency. Furthermore, any component that increases solution viscosity (e.g., excess metaborate) may reduce the hydrogen gas production rate. Based on the experimental findings for catalyst dosage and initial $NaBH_4$ concentration, the rate law equations were derived

$$\frac{-4d[NaBH_4]}{dt} = \frac{d[H_2]}{dt} = k[Fe/Glu]^{0.58}[NaBH_4]^{0.56} \tag{1}$$

$$\frac{-4d[NaBH_4]}{dt} = \frac{d[H_2]}{dt} = k[Ni/Glu]^{0.94}[NaBH_4]^{0.55} \tag{2}$$

As demonstrated, the overall reaction order of the hydrolysis reaction was determined to be approximately 1 and 1.5 for Fe/Glu and Ni/Glu catalysts, respectively. The Arrhenius equation was applied to calculate the activation energy of the reactions for both catalysts. To apply the Arrhenius equation, the rate constant (k) for the sodium borohydride hydrolysis reaction must first be determined. This rate constant exhibits temperature dependence, and thus, reactions were performed using fixed amounts of sodium borohydride ($NaBH_4$) and catalyst at varying temperatures (308, 318, and 328 K).

As shown in Fig. 9, the hydrogen gas production profiles revealed a significant enhancement in hydrogen generation with increasing temperature. Using the reaction rates obtained from catalyst dosage and $NaBH_4$ concentration experiments, the rate constants at the studied temperatures were calculated and subsequently used to derive the activation energies. For the Fe/Glu system, the rate constant was observed to increase by over 1.4-fold when the temperature was raised from 308 to 318 K, and by 2.6-fold at 328 K. In contrast, for the Ni/Glu catalyst, the rate constant increased by 2.5-fold and 6.3-fold under the same temperature increments. These results indicate that the temperature dependence of the hydrogen generation rate is more pronounced for the Ni/Glu catalyst compared to Fe/Glu. To determine the activation energy, the ln k diagram was drawn in 1/T.

The activation energy of the hydrolysis process was determined using the rate constant values and the respective catalysts. Fig. 8 also presents the Arrhenius plots for the hydrolysis of sodium borohydride using Fe/Glu and Ni/

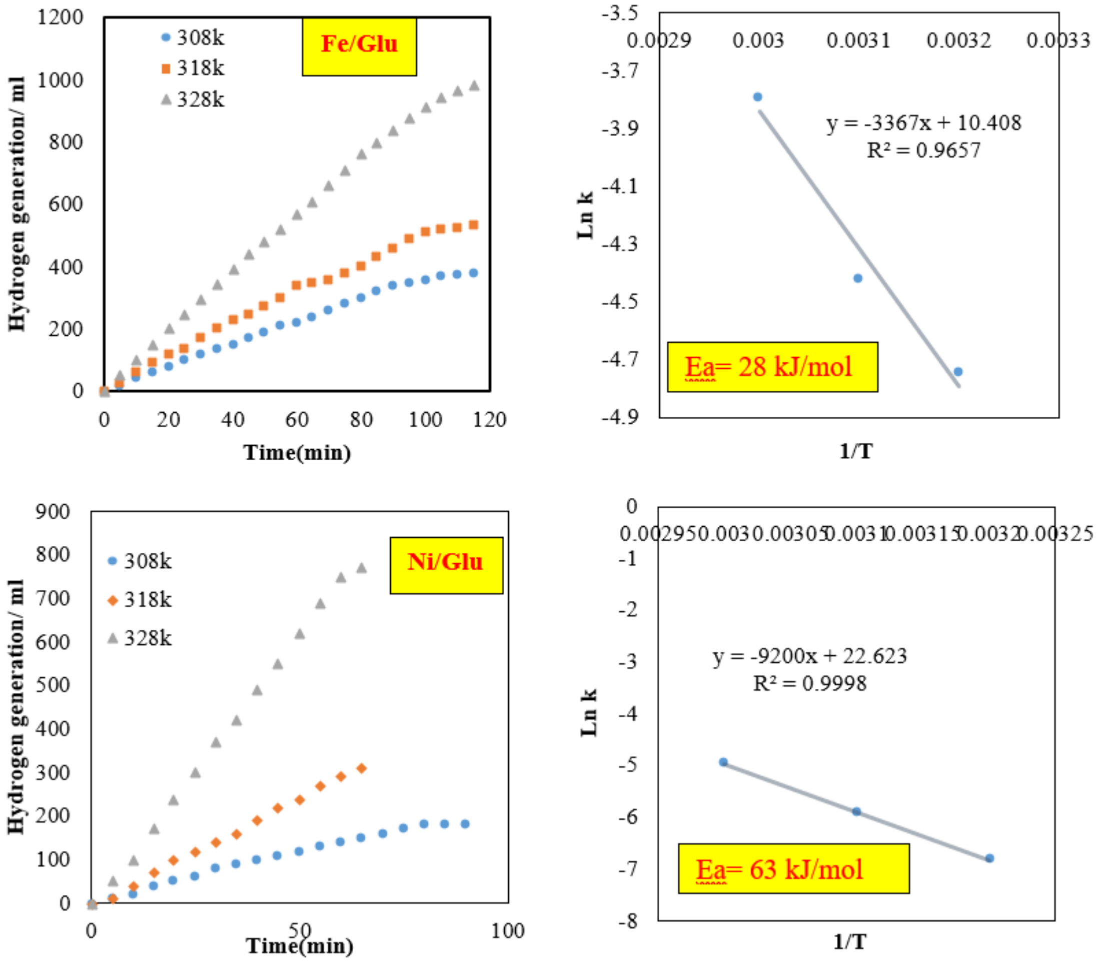

Fig. 9. The volume of hydrogen generated versus time and Arrhenius plot at different temperatures for the hydrolysis of $NaBH_4$ (5 wt.%) and 50 mg catalyst.

Glu catalysts. The activation energies for both catalysts were calculated from the slopes of their respective Arrhenius plots. Derived from these plots, the activation energy values for Fe/Glu and Ni/Glu were found to be 28 $kJ\cdot mol^{-1}$ and 63 $kJ\cdot mol^{-1}$, respectively. The temperature-dependent kinetic parameters and associated statistical analysis are summarized in Table 1, highlighting the catalyst's enhanced activity with rising thermal energy. The kinetic investigation across varying temperatures reveals a significant enhancement in reaction rates with increasing thermal energy, consistent with Arrhenius-type behavior.

This trend underscores the thermally activated nature of the catalytic process, where elevated temperatures reduce activation barriers, thereby accelerating the reaction. The high reproducibility of the measurements is evidenced by low relative standard deviations across triplicate trials, affirming the robustness of the experimental methodology.

Notably, the highest tested temperature yielded the most favorable reaction rates, suggesting its potential for industrial adoption. These findings emphasize the critical role of thermal energy in modulating catalytic efficiency, providing a foundation for optimizing reaction conditions in scalable applications.

The relationship between reaction rate and temperature can be established using the Arrhenius and Eyring equations. The Eyring equation, rooted in statistical thermodynamics, is based

Table 1. Kinetic constants at varying temperatures for Fe/Glu catalyst.

Temperature (K)	Mean ± SD (k)	RSD
308	0.00874 ± 0.000262	~3%
318	0.01205 ± 0.00036	~3%
328	0.0226 ± 0.00091	~4%

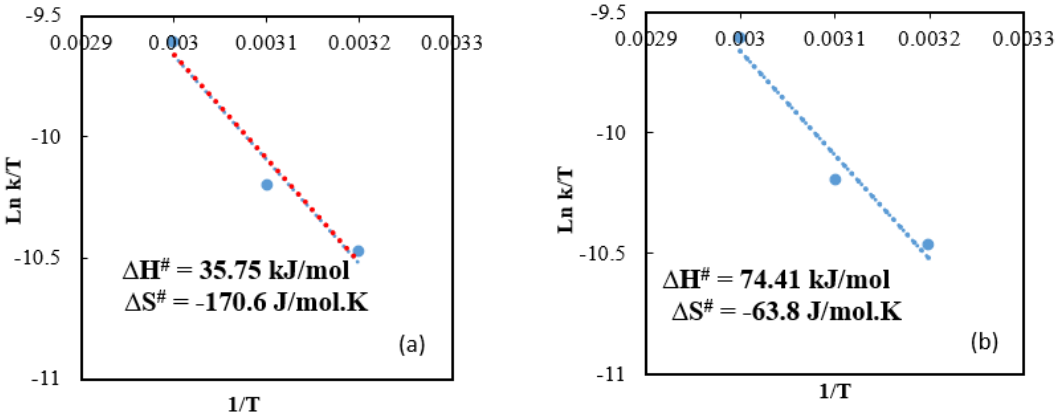

Fig. 10. Eyring plots of **(a)** Fe/Glu and **(b)** Ni/Glu

on transition state theory, whereas the Arrhenius equation is empirical. The activation energy of the reaction at various temperatures is obtained from the Arrhenius equation, whereas the Eyring equation is used to estimate the activation enthalpy (**ΔH‡**) and activation entropy (**ΔS‡**).

$$k = Ae^{-\frac{E_a}{RT}} \quad (3)$$

$$Lnk = LnA - \frac{E_a}{RT} \quad (4)$$

$$Ln\left(\frac{k}{T}\right) = Ln\left(\frac{k_B}{h}\right) + \frac{\Delta S^{\#}}{R} - \left(\frac{\Delta H^{\#}}{R}\right)\left(\frac{1}{T}\right) \quad (5)$$

In equations (3), (4) and (5), k is the rate constants, A is pre-exponential factor, Ea is the activation energy, T is the temperature in Kelvin, R is the gas constant 8.314 J/molK), kB is the Boltzmann constant (1.38 × 10-23 J/K), h is the Planck constant (6.63 × 10-34 J·s), ΔS# is the activation entropy, and ΔH# is the activation enthalpy. The corresponded diagrams are shown in Figure 10. Negative activation entropy can be attributed to the adsorption of water and sodium borohydride molecules at the rate determining step on the catalyst surface. Therefore, the total number of molecules in the rate determining step decreases.

Table 2 shows activation energies of several catalysts for hydrogen generation reaction.

The results confirm that the glucomannan-based Fe catalyst developed in this work exhibits high catalytic activity for hydrogen generation via the hydrolysis of $NaBH_4$ solution. The activation energy (E_a) of the Fe/Glu catalyst was found to be slightly higher than those reported for Fe_2O_3-decorated oxidized MWCNTs [27] and Co-W-P/Cu sheet [74], while being comparable to Co-Ni-P-B [75], Co–Fe–B [29], and PVP-protected Au/Ni [76]. In contrast, higher E_a values were observed for Co–Ni–B [77], Co–Ni–P film [78], Co-Ni-B/Cu sheet [79], Co-Ni-Fe-P [31], $NiCo_2O_4$/zeolite [80], Co/SiO_2 [47], and Ni–Co–B [12] catalysts compared to the Fe/Glu catalyst. Notably, the E_a value of the Ni/Glu catalyst was lower than that of Fe/Glu, which is consistent with the TEM analysis. The TEM images revealed that the average particle size of Fe stabilized with the polymer was approximately 11 nm, whereas Ni particles were significantly larger (~256 nm). It is well-established that smaller particle sizes correspond to larger

Table 2. Activation energy values for the hydrolysis of $NaBH_4$ solution catalyzed by various catalysts published previously.

Catalyst	Ea (kJ / mol)	Ref.
Fe_2O_3 decorated oxidized MWCNTs	15.92	[27]
Co-W-P/Cu sheet	22.8	[74]
Co-Ni-P-B	29	[75]
Co–Fe–B	29.09	[29]
PVP-protected Au/Ni	30.3	[76]
Co–Ni–B	34	[77]
Co–Ni–P film	38	[78]
Co-Ni-B/Cu sheet	42.8	[79]
Co-Ni-Fe-P	54.26	[31]
$NiCo_2O_4$/zeolite	55.79	[80]
Co/SiO_2	59	[47]
Ni–Co–B	62	[12]
Fe/Glu	28	This work
Ni/Glu	63	This work

surface areas, thereby increasing surface energy and reducing the activation energy required for surface-mediated reactions. As demonstrated in Table 2 and throughout this study, the Fe/Glu catalyst exhibits remarkable efficiency for hydrogen production via $NaBH_4$ hydrolysis.

The combination of low activation energy, cost-effectiveness, abundance, and high catalytic activity renders the glucomannan-based Fe catalyst a unique candidate for hydrogen generation. In this work, hydrogen production via $NaBH_4$ hydrolysis was investigated using a heterogeneous catalyst, where surface adsorption plays a critical role. The reaction mechanism involves three key steps: adsorption of reactants onto the catalyst surface, surface diffusion, and desorption of products. As illustrated in Scheme 3, water molecules are adsorbed onto electron-deficient sites (e.g., Fe-B species), while BH_4^- anions are adsorbed onto electron-rich sites (e.g., Fe metal). During this process, a lone pair of electrons from water oxygen is transferred to the partially positive sites on the catalyst surface, and a hydrogen atom from water combines with a hydride from BH_4^- to form molecular hydrogen. This mechanism ultimately yields four hydrogen molecules per $NaBH_4$ molecule.

The combination of low activation energy, cost-effectiveness, abundance, and high catalytic activity renders the glucomannan-based Fe catalyst a unique candidate for hydrogen generation. In this work, hydrogen production via $NaBH_4$ hydrolysis was investigated using a heterogeneous catalyst, where surface adsorption plays a critical role. The reaction mechanism involves three key steps: adsorption of reactants onto the catalyst surface, surface diffusion, and desorption of products. As illustrated in Scheme 3, water molecules are adsorbed onto electron-deficient sites (e.g., Fe-B species), while BH_4^- anions are adsorbed onto electron-rich sites (e.g., Fe metal). During this process, a lone pair of electrons from water oxygen is transferred to the partially positive sites on the catalyst surface, and a hydrogen atom from water combines with a hydride from BH_4^- to form molecular hydrogen. This mechanism ultimately yields four hydrogen molecules per $NaBH_4$ molecule.

The reusability of the Fe/Glu catalyst is illustrated in Fig. 11. The catalyst exhibited a gradual decline in activity across successive runs, with the most pronounced reduction observed between the

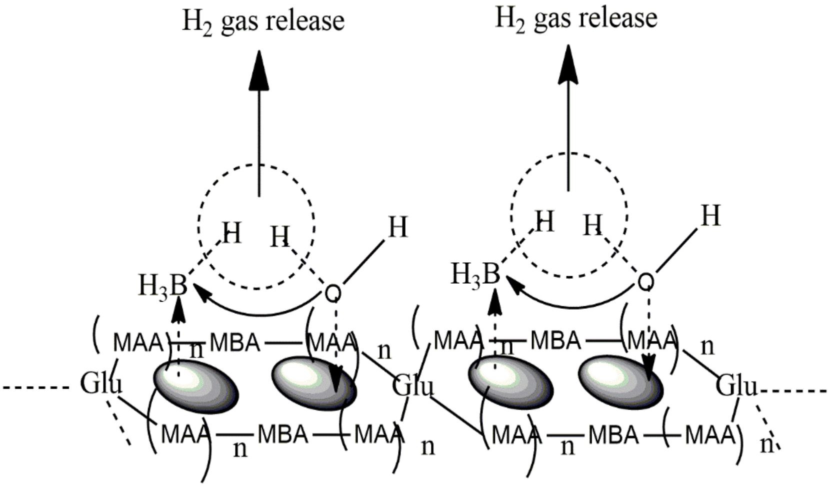

Scheme 3. Proposed mechanism for hydrolysis of NaBH4 over glucomannan-based nano catalyst

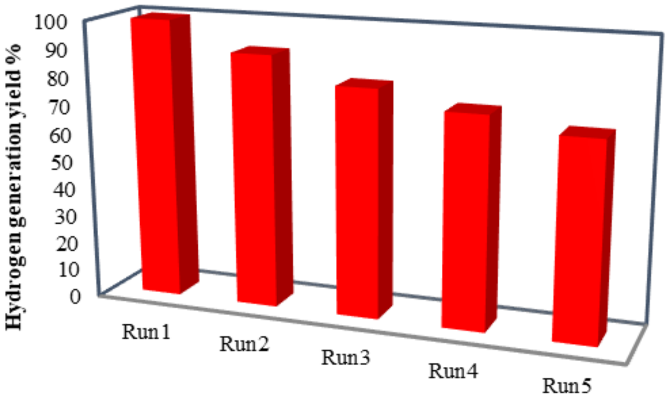

Fig 11. Reusability of the Fe/Glu catalyst

initial and subsequent cycles. This trend reflects progressive deactivation mechanisms inherent to repeated catalytic processes. Notably, the rate of activity loss stabilized in later runs, suggesting partial retention of active sites or structural integrity under operational stress. The observed behavior aligns with the kinetic stability inferred from earlier thermodynamic analyses, where the core-shell morphology and robust polymer-metal interactions likely mitigated rapid degradation. The catalyst maintained functional efficacy throughout multiple cycles, underscoring its suitability for applications prioritizing cost-effective reuse over peak single-cycle performance. This recyclability profile, consistent with the structural insights from TEM and XPS characterization, reinforces the design rationale for biopolymer-supported catalytic systems.

4. Conclusions

Extracted glucomannan, a biodegradable polysaccharide derived from *Orchis mascula* roots, was employed to immobilize Fe and Ni nanoparticles via a facile reduction process. Using N,N'-methylenebisacrylamide (MBA) as a cross-linker and methacrylic acid (MAA) as a monomer, an insoluble polymer matrix was synthesized, effectively stabilizing the metal particles. TEM analysis revealed a core-shell structure, where glucomannan chains encapsulated Fe nanoparticles with an average size of 11 nm, while Ni particles exhibited significantly larger dimensions (~256 nm). The catalytic efficacy of Fe/Glu and Ni/Glu was evaluated for hydrogen generation via NaBH$_4$ hydrolysis, yielding overall reaction orders of ~1 and ~1.5, respectively. The Fe/Glu catalyst demonstrated superior performance, evidenced by its low activation energy (28 kJ/mol vs. 63 kJ/mol for Ni/Glu) and favorable thermodynamic parameters ($\Delta H^{\ddagger} = 35.75$ kJ/mol; $\Delta S^{\ddagger} = -170.6$ J/mol·K). The use of glucomannan as a renewable, non-toxic biopolymer support underscores the catalyst's alignment with green chemistry principles, reducing reliance on synthetic materials and minimizing ecological risks associated with conventional catalyst synthesis. The Fe/Glu system's ability to operate under mild conditions (ambient temperature/pressure) significantly lowers energy consumption compared to high-temperature industrial processes. Furthermore, the absence of noble metals eliminates dependency on scarce resources, enhancing sustainability. The core-shell architecture not only prevents nanoparticle agglomeration but also ensures long-term stability, making the catalyst suitable for scalable industrial applications such as fuel cells or portable hydrogen generators. This work highlights the potential of biopolymer-supported catalysts to advance clean energy technologies, bridging fundamental research with environmentally conscious, practical solutions for global hydrogen production challenges.

Acknowledgments

The authors are grateful to the Research Council of University of Guilan for the partial support of this study.

Conflicts of interest

The authors declare no competing interests.

References

[1] S. Özkar, Transition metal nanoparticle catalysts in releasing hydrogen from the methanolysis of ammonia borane, Int. J. Hydrogen. Energy. 45 (2020) 7881-7891. https://doi.org/10.1016/j.ijhydene.2019.04.125.

[2] X. Wang, Ch. Wu, Y. Zhang, Y. Chen, Hydrogen generation behaviors of LiAlH$_4$ and NH$_4$Cl in Et$_2$O, THF or DME, Int. J. Hydrogen. Energy. 41 (2016) 6825-6832. https://doi.org/10.1016/j.ijhydene.2016.03.081.

[3] A. Karabulut, M.S. İzgi, H. Demir, O. Sahin, S. Horoz, Optimizing hydrogen production from alkali hydrides using supported metal catalysts, Ionics. 29 (2023) 1975–1982. https://doi.org/10.1007/s11581-023-04962-8.

[4] O.V. Netskina, E.S. Tayban, V.A. Rogov, A.M. Ozerova, S.A. Mukha, V.I. Simagina, O.V. Komova Solid-state NaBH$_4$ composites for hydrogen generation: Catalytic activity of nickel and cobalt catalysts, Int. J. Hydrogen. Energy. 46 (2021) 5459-5471. https://doi.org/10.1016/j.ijhydene.2020.11.078.

[5] Y. Kojima, Y. Kawai, H. Nakanishi, Sh. Matsumoto, Compressed hydrogen generation using chemical hydride, J. Power Sources. 135 (2004) 36-41. https://doi.org/10.1016/j.jpowsour.2004.03.079.

[6] H.N. Abdelhamid, A review on hydrogen generation from the hydrolysis of sodium borohydride, Int. J. Hydrogen. Energy. 46 (2021) 726-765. https://doi.org/10.1016/j.ijhydene.2020.09.186.

[7] Ch. Wu, F. Wu, Y. Bai, B.Yi, H. Zhang, Cobalt boride catalysts for hydrogen generation from alkaline NaBH$_4$ solution, Mater. Lett. 59 (2005) 1748-1751. https://doi.org/10.1016/j.matlet.2005.01.058.

[8] L. Wang, Zh. Li, Y. Zhang, T. Zhang, G. Xie Hydrogen generation from alkaline NaBH$_4$ solution using electroless-deposited Co–Ni–W–P/γ-Al$_2$O$_3$ as catalysts. J. Alloys Compd 702 (2017) 649-658. https://doi.org/10.1016/j.jallcom.2017.01.295.

[9] Y. Wang, Y. Lu, D. Wang, Sh.Wu, Zh. Cao, K. Zhang, H. Liu, Sh. Xin, Hydrogen generation from hydrolysis of sodium borohydride using nanostructured Ni-B catalysts, Int. J. Hydrogen. Energy. 41 (2016) 16077- 16086. https://doi.org/10.1016/j.ijhydene.2016.05.258.

[10] J.H. Kim, K.T. Kim, Y.M. Kang, H.S. Kim, M.S. Song, Y.J Lee, P.S. Lee, J.Y. Lee, Study on degradation of filamentary Ni catalyst on hydrolysis of sodium borohydride, J. Alloys Compd. 379 (2004) 222-227. https://doi.org/10.1016/ j.jallcom.2004.02.009.

[11] Sh. A. Al-Thabaiti, Z. Khan, M.A. Malik, Bimetallic Ag-Ni nanoparticles as an effective catalyst for hydrogen generation from hydrolysis of sodium borohydride, Int. J. Hydrogen. Energy. 44 (2019) 16452-16466. https://doi.org/10.1016/j.ijhydene.2019.04.240.

[12] J.C. Ingersoll, N. Mani, J.C. Thenmozhiyal, A. Muthaiah Catalytic hydrolysis of sodium borohydride by a novel nickel–cobalt–boride catalyst, J. Power Sources.173 (2007) 450-457. https://doi.org/10.1016/j.jpowsour.2007.04.040.

[13] M. Nie, Y.C. Zou, Y.M. Huang, J.Q. Wang, Ni-Fe-B catalysts for NaBH$_4$ hydrolysis, Int. J. Hydrogen. Energy. 37 (2012) 1568- 1576. https://doi.org/10.1016/j.ijhydene.2011.10.006.

[14] Y. Chen, H. Kim, Use of a nickel-boride–silica nanocomposite catalyst prepared by in-situ reduction for hydrogen production from hydrolysis of sodium borohydride, Fuel Process. Technol. 89 (2008) 966-972. https://doi.org/10.1016/j.fuproc.2008.04.005.

[15] A.H. Didehban, M. Zabihi, J.R. Shahrouzi, Experimental studies on the catalytic behavior of alloy and core-shell supported Co-Ni bimetallic nano-catalysts for hydrogen generation by hydrolysis of sodium borohydride, Int. J. Hydrogen. Energy. 43 (2018) 20645-20660. https://doi.org/10.1016/j.ijhydene.2018.09.127.

[16] Y. Li, X. Hou, J. Wang, X. Feng, L. Cheng, H. Zhang, Sh. Han, Co-Mo nanoparticles loaded on three-dimensional graphene oxide as efficient catalysts for hydrogen generation from catalytic hydrolysis of sodium borohydride, Int. J. Hydrogen. Energy. 44 (2019) 29075- 29082. https://doi.org/10.1016/j.ijhydene.2019.02.124.

[17] D. Aman, A.A. Alkahlawy, T. Zaki, Hydrolysis of NaBH$_4$ using ZVI/Fe$_2$(MoO$_4$)$_3$ nanocatalyst, Int. J. Hydrogen. Energy. 43 (2018) 18289-18295. https://doi.org/10.1016/j.ijhydene.2018.08.078.

[18] H.N. Abdelhamid, Salts Induced Formation of Hierarchical Porous ZIF-8 and Their applications for CO$_2$ Sorption and Hydrogen Generation via NaBH$_4$ Hydrolysis, Macromol. Chem. Phys. 21 (2020) 2000031. https://doi.org/10.1002/macp.202000031.

[19] Y. Wei, X. Huang, J. Wang, H. Yu, X. Zhao, D. Cheng, Synthesis of bi functional non-noble monolithic catalyst

Co-W-P/carbon cloth for sodium borohydride hydrolysis and reduction of 4-nitrophenol, Int. J. Hydrogen. Energy. 42 (2017) 25860-25868. https://doi.org/10.1016/j.ijhydene.2017.08.148.

[20] H. Ma, W. Ji, J. Zhao, J, Liang, J, Chen, Preparation, characterization and catalytic $NaBH_4$ hydrolysis of Co-B hollow spheres, J. Alloys Compd. 474 (2009) 584–589. https://doi:10.1016/j.jallcom.2008.07.005.

[21] X. Yuan, Ch. Jia, X.L. Ding, Z.F. Ma, Effects of heat-treatment temperature on properties of Cobalt-Manganese-Boride as efficient catalyst toward hydrolysis of alkaline sodium borohydride solution, Int. J. Hydrogen. Energy. 37 (2012) 995-1001. https://doi.org/10.1016/j.ijhydene.2011.03.064.

[22] Y. Zou, Y. Yin, Y. Gao, C. Xiang, H. Chu, Sh. Qiu, E. Yan, F. Xu, L. Sun, Chitosan-mediated Co-Ce-B nanoparticles for catalyzing the hydrolysis of sodium borohydride, Int. J. Hydrogen. Energy. 43 (2018) 4912-4921. https://doi.org/10.1016/j.ijhydene.2018.01.125.

[23] Y. Wei, M. Wang, W. Fu, L. Wei, X. Zhao, X. Zhou, M Ni, H. Wang, Highly active and durable catalyst for hydrogen generation by the $NaBH_4$ hydrolysis reaction: CoWB/NF nanodendrite with an acicular array structure, J. Alloys Compd. 836 (2020) 155429-155437. https://doi.org/10.1016/j.jallcom.2020.155429.

[24] K. Li, M. Ma, L. Xie, Y. Yao, R. Kong, G. Du, A.M. Asiri, X. Sun, Monolithically integrated Ni Co P nanosheet array on Ti mesh: An efficient and reusable catalyst in $NaBH_4$ alkaline media toward on-demand hydrogen generation, Int. J. Hydrogen. Energy. 42 (2017) 19028-19034. https://doi.org/10.1016/j.ijhydene.2017.06.092.

[25] A.A. Vernekar, S.T. Bugde, S. Tilve, Sustainable hydrogen production by catalytic hydrolysis of alkaline sodium borohydride solution using recyclable Co–Co_2B and Ni–Ni_3B nanocomposites, Int. J. Hydrogen. Energy. 37 (2012) 327-334. https://doi.org/10.1016/j.ijhydene.2011.09.033.

[26] A.F. Baye, M.W. Abebe, R. Appiah-Ntiamoah, H. Kim, Engineered iron-carbon-cobalt (Fe_3O_4@C-Co) core-shell composite with synergistic catalytic properties towards hydrogen generation via $NaBH_4$ hydrolysis, J. Colloid Interface Sci. 543 (2019) 273-284. https://doi.org/10.1016/j.jcis.2019.02.065.

[27] D. Prasad, K.N. Patil, N. Sandhya, C.R. Chaitra, J.T. Bhanushali, A.K. Samal, R.S. Keri, A.H. Jadhav, B.M. Nagaraja, highly efficient hydrogen production by hydrolysis of $NaBH_4$ using eminently competent recyclable Fe_2O_3 decorated oxidized MWCNTs robust catalyst, Appl. Surf. Sci. 489 (2019) 538-551. https://doi.org/10.1016/j.apsusc.2019.06.041.

[28] M.H. Loghmani, A. FallahShojaei, M. Khakzad, Hydrogen generation as a clean energy through hydrolysis of sodium borohydride over Cu-Fe-B nano powders: Effect of polymers and surfactants, Energy. 126 (2017) 830-840. https://doi.org/10.1016/j.energy.2017.03.006.

[29] Y.P. Wang, Y.J. Wang, Q.L. Ren, L. Li, L.F. Jiao, D.W. Song, G. Liu, Y. Han, H.T. Yuan, Ultrafine Amorphous Co–Fe–B Catalysts for the Hydrolysis of $NaBH_4$ Solution to Generate Hydrogen for PEMFC, Fuel Cells. 10 (2010) 132-138. https://doi.org/10.1002/fuce.200900091.

[30] Y. Zhang, X. Wang, Ch. Yao, G. Qin, Preparation and Characterization of Amorphous Fe-B-P Ultrafine Particles, Mater. Sci. Forum. 848 (2016) 652-656. https://doi.org/10.4028/www.scientific.net/MSF.848.652.

[31] D.H. Kim, S. Jo, J. Kwon, Se. Lee, K.S. Eom, Effect of iron content on the hydrogen production kinetics of electroless-deposited Co-Ni-Fe-P alloy catalysts from the hydrolysis of sodium borohydride, and a study of its feasibility in a new hydrolysis using magnesium and calcium borohydrides, Int. J. Hydrogen. Energy. 44 (2019) 15228-15238. https://doi.org/10.1016/j.ijhydene.2019.04.169.

[32] M.S. Keskin, M.S. Agırtaş, Hydrogen production performance and kinetic behavior from sodium borohydride hydrolysis with TiO_2-supported Co-Mo-B catalyst, Ionics. 29 (2023) 3713–3721. https://doi.org/10.1007/s11581-023-05102-y.

[33] A. Chinnappan, J.M.C. Puguan, W.J. Chung, H. Kim, Hydrogen generation from the hydrolysis of sodium borohydride using chemically modified multiwalled carbon nanotubes with pyridinium based ionic liquid and decorated with highly dispersed Mn nanoparticles, J. Power Sources. 293 (2015) 429-436. https://doi.org/10.1016/j.jpowsour.2015.05.096.

[34] N. Sahiner, A.O. Yasar, Imidazolium based polymeric ionic liquid microgels as an alternative catalyst to metal catalysts for H_2 generation from methanolysis of $NaBH_4$, Technol 152 (2016) 316-324. https://doi.org/10.1016/j.fuproc.2016.06.023.

[35] M. Soltani, M. Zabihi, Hydrogen generation by catalytic hydrolysis of sodium borohydride using the nano-bimetallic catalysts supported on the core-shell magnetic nanocomposite of activated carbon, Int. J. Hydrogen Energy. 45 (2020) 12331-12346. https://doi.org/10.1016/j.ijhydene.2020.02.203

[36] H.A. Bandal, A.R. Jadhav, H. Kim, Cobalt impregnated magnetite-multiwalled carbon nanotube nanocomposite as magnetically separable efficient catalyst for hydrogen generation by $NaBH_4$ hydrolysis, J. Alloys Compd. 699 (2017) 1057-1067. https://doi.org/10.1016/j.jallcom.2016.12.428.

[37] A. Chinnappan, A.H. Jadhav, J.M.C Puguan, R.A. Ntiamoah, H. Kim, Fabrication of ionic liquid/polymer nanoscale networks by electrospinning and chemical cross-linking and their application in hydrogen generation from the hydrolysis of $NaBH_4$, Energy. 79 (2015) 482-488. https://doi.org/10.1016/j.energy.2014.11.041.

[38] T. Turhan, Y.A. Güvenilir, N. Sahiner, Micro poly(3-sulfopropyl methacrylate) hydrogel synthesis for in situ metal nanoparticle preparation and hydrogen generation from hydrolysis of $NaBH_4$, Energy. 55 (2013) 511- 518. https://doi.org/10.1016/j.energy.2013.01.035.

[39] J. Ding, Q. Li, Y. Su, Q. Yue, B. Gao, W. Zhou, Preparation and catalytic activity of wheat straw cellulose based hydrogel-nanometal composites for hydrogen generation from $NaBH_4$ hydrolysis, Int. J. Hydrogen. Energy. 43 (2018) 9978-9987. https://doi.org/10.1016/j.ijhydene.2018.04.077.

[40] S. Demirci, N. Sahiner, Superior reusability of metal catalysts prepared within poly(ethylene imine) microgels for H_2 production from $NaBH_4$ hydrolysis, Fuel Process Technol. 127 (2014) 88-96. https://doi.org/10.1016/j.fuproc.2014.06.013.

[41] I. Kıpcak, E. Kalpazan, Preparation of CoB catalysts supported on raw and Na-exchanged bentonite clays and their application in hydrogen generation from the hydrolysis of $NaBH_4$, Int. J. Hydrogen Energy. 45 (2020) 26434- 26444. https://doi.org/10.1016/j.ijhydene.2020.03.230.

[42] F. Wang, Y. Zhang, Y. Wang, Y. Luo, Y. Chen, H. Zhu, Co-P nanoparticles supported on dandelion-like CNTs-Ni foam composite carrier as a novel catalyst for hydrogen generation from $NaBH_4$ methanolysis, Int. J. Hydrogen. Energy. 43 (2018) 8805-8814. https://doi.org/10.1016/j.ijhydene.2018.03.140.

[43] C. Saka, M.S Eygi, A. Balbay, CoB doped acid modified zeolite catalyst for enhanced hydrogen release from sodium borohydride hydrolysis, Int. J. Hydrog. Energy. 45 (2020) 15086- 15099. https://doi.org/10.1016/j.ijhydene.2020.03.238.

[44] F. Seven, N. Sahiner, Enhanced catalytic performance in hydrogen generation from NaBH4 hydrolysis by super porous cryogel supported Co and Ni catalysts, J. Power Sources. 272 (2014) 128-136. https://doi.org/10.1016/j.jpowsour.2014.08.047.

[45] F. Li, E.E. Arthur, D. La, Q. Li, H. Kim, Immobilization of CoCl$_2$ (cobalt chloride) on PAN (polyacrylonitrile) composite nanofiber mesh filled with carbon nanotubes for hydrogen production from hydrolysis of NaBH$_4$ (sodium borohydride), Energy. 71 (2014) 32-39. https://doi.org/10.1016/j.energy.2014.03.130.

[46] F. Li, Q. Li, H. Kim, CoB/open-CNTs catalysts for hydrogen generation from alkaline NaBH$_4$ solution, Chem. Eng. J. 210 (2012) 316-324. https://doi.org/10.1016/j.cej.2012.08.102.

[47] Y.J. Shih, Ch.Ch. Su, Y.H. Huang, MCh. Lu, SiO$_2$-supported ferromagnetic catalysts for hydrogen generation from alkaline NaBH$_4$ (sodium borohydride) solution, Energy. 54 (2013) 263-270, https://doi.org/10.1016/j.energy.2013.01.063.

[48] Q. Li, H. Kim, Hydrogen production from NaBH$_4$ hydrolysis via Co-ZIF-9 catalyst, Fuel. Process. Technol. 100 (2012) 43-48. https://doi.org/10.1016/j.fuproc.2012.03.007.

[49] H.N. Abdelhamid, Dehydrogenation of sodium borohydride using cobalt embedded zeolitic imidazolate frameworks, J. Solid. State. Chem. 297 (2021) 122034-122042. https://doi.org/10.1016/j.jssc.2021.122034.

[50] K.Y.A Lin, H.A. Chang, Efficient hydrogen production from NaBH$_4$ hydrolysis catalyzed by a magnetic cobalt/carbon composite derived from a zeolitic imidazolate framework. Chem. Eng. J 296 (2016) 243-251. https://doi.org/10.1016/j.cej.2016.03.115.

[51] W. Niu, D. Ren, Y. Han, Y. Wu, X. Gou, optimizing preparation of carbon supported cobalt catalyst for hydrogen generation from NaBH$_4$ hydrolysis, J. Alloys Compd. 543 (2012) 159-166. http://dx.doi.org/10.1016/j.jallcom.2012.07.099.

[52] N. Sahiner, A.O. Yasar, Synthesis and modification of p(VI) microgels for in situ metal nanoparticle preparation and their use as catalyst for hydrogen generation from NaBH$_4$ hydrolysis, Fuel. Process. Technol. 111 (2013) 14-21. https://doi.org/10.1016/j.fuproc.2012.09.064.

[53] N. Sahiner, A.O. Yasar, H$_2$ generation from NaBH$_4$ and NH$_3$BH$_3$ using metal catalysts prepared within p(VI) capsule particles, Fuel Process. Technol. 125 (2014) 148-154. https://doi.org/10.1016/j.fuproc.2014.03.037.

[54] F. Seven, N. Sahiner, Modified macroporous P(2-hydroxyethyl methacrylate) P(HEMA) cryogel composites for H$_2$ production from hydrolysis of NaBH$_4$, Fuel. Process. Technol. 128 (2014) 394-401. https://doi.org/10.1016/j.fuproc.2014.08.008.

[55] A. Kurt, A. Cengiz, T. Kahyaoglu, The effect of gum tragacanth on the rheological properties of salep based ice cream mix, Carbohydr. Polym. 143 (2016) 116-115. https://doi.org/10.1016/j.carbpol.2016.02.018

[56] A. Pourjavadi, M. Doulabi, R. Soleyman, S. Sharif, S.A. Eghtesadi, Synthesis and characterization of a novel (salep phosphate)-based hydrogel as a carrier matrix for fertilizer release, React, Funct. Polym. 72 (2012) 667-672. https://doi.org/10.1016/j.reactfunctpolym.2012.06.010.

[57] M.H. Loghmani, A. Fallah-Shojaei, Synthesis and characterization of Co–La–Zr–B quaternary amorphous nano alloy: Kinetic study for hydrogen generation from hydrolysis of sodium borohydride, J. Alloys Compd. 580 (2013) 61- 66. https://doi.org/10.1016/j.jallcom.2013.05.078.

[58] M.H. Loghmani, A. Fallah-Shojaei, Hydrogen generation from hydrolysis of sodium borohydride by cubic Co-La-Zr-B nano particles as novel catalyst, Int. J. Hydrogen Energy. 38 (2013) 10470-10478. https://doi.org/10.1016/j.ijhydene.2013.05.141.

[59] M.H. Loghmani, A. Fallah-Shojaei, Hydrogen production through hydrolysis of sodium borohydride: Oleic acid stabilized Co-La-Zr-B nanoparticle as a novel catalyst, Energy. 68 (2014) 152-159. https://doi.org/10.1016/j.energy.2014.02.047.

[60] M.H. Loghmani, A. Fallah-Shojaei, Reduction of cobalt ion improved by lanthanum and zirconium as a triphenylphosphine stabilized nano catalyst for hydrolysis of sodium borohydride, Int. J. Hydrog. Energy. 40 (2015) 6573-6581. https://doi.org/10.1016/j.ijhydene.2015.03.116.

[61] M.H. Loghmani, Various Rate Law Orders Through Hydrolysis of Sodium Borohydride Over Co-M-Zr-B (M= Cr, Mo and W) Nano Catalyst, Int. J. Chemoinfo. Chem. Eng. 6 (2017) 45-61. 10.4018/IJCCE.2017070104.

[62] M.H. Loghmani, A. Fallah-Shojaei, Effect of preparation temperature and ions doping on size, morphology and catalytic activity of Co-B amorphous nano catalyst, Bull. Chem. Soc. Ethiop. 29 (2015) 105-116. https://doi.org/10.4314/bcse.v29i1.9.

[63] M.H. Loghmani, M. Jalali-rad, Hydrogen generation via cross-linked glucomannan supported cobalt nano catalyst, Int. J. Hydrogen Energy. 46 (2021) 36137-36151. https://doi.org/10.1016/j.ijhydene.2021.08.124.

[64] B.M. Lanté, R. Djenadic, V.S.K. Chakravadhanula, Ch. Kübel, V.V. Srdić, H. Hahn, Chemical Vapor Synthesis of FeOx–BaTiO$_3$ Nanocomposites, J. Am. Ceram. Soc. 98 (2015) 1724-1730. https://doi: 10.1111/jace.13531.

[65] V.I. Dybkov, W. Lengauer, P. Gas, Formation of boride layers at the Fe–25% Cr alloy–boron interface, J. Mater. Sci. 41(2006) 4948-4960. https://doi.org/ 10.1007/s10853-006-0032-9

[66] C. Maritini, G. palombarini , Mechanism of thermochemical growth of iron borides on iron, J. Mater. Sci. 39 (2004) 933- 937. https://doi.org/10.1023/B:JMSC.0000012924.74578.87.

[67] B.Y. Yu, S.Y. Kwak, Assembly of magnetite nanocrystals into spherical mesoporous aggregates with a 3-D wormhole-like pore structure, J. Mater. Chem. 20 (2010) 8320-8328. https://doi.org/10.1039/C0JM01274B.

[68] Y. Cheng, M. Tanaka, T.Watanabe, S.Y. Choi, M.S. Shin, K.H. Lee, Synthesis of Ni$_2$B nanoparticles by RF thermal plasma for fuel cell catalyst, J. Phys. Conf. Ser. 518 (2014) 012026. https://doi.org/10.1088/1742-6596/518/1/012026.

[69] L. Liu, H. Zhang, L. Fang, Y. Mu, Y.Wang, Facile preparation of novel dandelion-like Fe-doped NiCo$_2$O$_4$ microspheres@nanomeshes for excellent capacitive property in asymmetric supercapacitors, J. Power. Sources. 327 (2016) 135-144. https://doi.org/10.1016/j.jpowsour.2016.07.054.

[70] B. Liu, B. Zheng, Y. Wang, H. Li, W. Wang, Performance evaluation of hierarchical and conductive fabric-based electrodes decorated with amorphous FeB nanosheets, Cellulose. 27 (2020) 8813-8825. https://doi.org/10.1007/s10570-020-03378-1.

[71] D. Fa, B. Yu, Y. Miao, Synthesis of ultra-long nanowires of nickel phosphate by a template-free hydrothermal method for electrocatalytic oxidation of glucose, Colloids Surf. A: Physicochem. Eng. Asp. 564 (2019) 31-38. https://doi.org/10.1016/j.colsurfa.2018.12.035.

[72] W. Liu, R. Chen, L. Liu, S. Li, Zh. Xue, C. He, Amorphous NiB/carbon nanohybrids: synthesis and catalytic enhancement induced by electron transfer, RSC Adv. 6 (2016) 94451-94458. https://doi.org/10.1039/C6RA19262A

[73] A. Kaur, D. Gangacharyulu, P.K. Bajpai, Kinetic studies of hydrolysis reaction of NaBH$_4$ with γ-Al$_2$O$_3$ nanoparticles as catalyst promotor and CoCl$_2$ as catalyst. Braz, J. Chem. Eng. 36 (2019) 929-939. https://doi.org/10.1590/0104-6632.20190362s20180290.

[74] Y. Guo, Zh. Dong, Zh. Cui, X. Zhang, J. Ma, Promoting effect of W doped in electrodeposited Co–P catalysts for hydrogen generation from alkaline NaBH$_4$ solution, Int J Hydrogen Energy. 37(2012) 1577- 1583. https://doi.org/10.1016/j.ijhydene.2011.10.019.

[75] R. Fernandes, N. Patel, A. Miotello, Efficient catalytic properties of Co–Ni–P–B catalyst powders for hydrogen generation by hydrolysis of alkaline solution of NaBH$_4$,

Int. J. Hydrogen Energy. 34 (2009) 2893-2900. https://doi.org/10.1016/j.ijhydene.2009.02.007.

[76] X. Wang, Sh. Sun, Z. Huang, H. Zhang, Sh. Zhang, Preparation and catalytic activity of PVP-protected Au/Ni bimetallic nanoparticles for hydrogen generation from hydrolysis of basic $NaBH_4$ solution, Int. J. Hydrogen. Energy. 39 (2014) 905-916. https://doi.org/10.1016/j.ijhydene.2013.10.122.

[77] R. Fernandes, N. Patel, A. Miotello, M. Filippi, Studies on catalytic behavior of Co–Ni–B in hydrogen production by hydrolysis of $NaBH_4$, J. Mol. Catal. A. Chem. 298 (2009) 1-6. https://doi.org/10.1016/j.molcata.2008.09.014.

[78] Y. Guo, Q. Feng, J. Ma, The hydrogen generation from alkaline $NaBH_4$ solution by using electroplated amorphous Co–Ni–P film catalysts, Appl. Surf. Sci 273 (2013) 253-256. https://doi.org/10.1016/j.apsusc.2013.02.025.

[79] Y. Wei, W. Meng, Y. Wang, Y. Gao, K. Qi, K. Zhang, Fast hydrogen generation from $NaBH_4$ hydrolysis catalyzed by nanostructured Co–Ni–B catalysts, Int. J. Hydrogen. Energy. 42 (2017) 6072-6079. https://doi.org/10.1016/j.ijhydene.2016.11.134.

[80] Y. Xin, Z. Wang, Y. Jiang, Kinetic study of $NaBH_4$ catalytic hydrolysis using supported $NiCo_2O_4$, Mater. Res. Express. 6 (2019) 1-11. https://doi.org/10.1088/2053-1591/ab5d4c.